

Fast current-driven domain walls and small skyrmions in a compensated ferrimagnet

Lucas Caretta^{1,5}, Maxwell Mann^{1,5}, Felix Büttner^{1,5}, Kohei Ueda¹, Bastian Pfau², Christian M. Günther^{2,3}, Piet Helsing², Alexandra Churikova¹, Christopher Klose², Michael Schneider², Dieter Engel², Colin Marcus¹, David Bono¹, Kai Bagschik⁴, Stefan Eisebitt^{2,3} and Geoffrey S. D. Beach^{1*}

Spintronics is a research field that aims to understand and control spins on the nanoscale and should enable next-generation data storage and manipulation. One technological and scientific key challenge is to stabilize small spin textures and to move them efficiently with high velocities. For a long time, research focused on ferromagnetic materials, but ferromagnets show fundamental limits for speed and size. Here, we circumvent these limits using compensated ferrimagnets. Using ferrimagnetic Pt/Gd₄₄Co₅₆/TaO_x films with a sizeable Dzyaloshinskii-Moriya interaction, we realize a current-driven domain wall motion with a speed of 1.3 km s⁻¹ near the angular momentum compensation temperature (T_A) and room-temperature-stable skyrmions with minimum diameters close to 10 nm near the magnetic compensation temperature (T_M). Both the size and dynamics of the ferrimagnet are in excellent agreement with a simplified effective ferromagnet theory. Our work shows that high-speed, high-density spintronics devices based on current-driven spin textures can be realized using materials in which T_A and T_M are close together.

Spin-based devices are being widely pursued for high-performance solid-state data storage and logic applications^{1–4}. A promising approach is to encode bits by nanoscale domain walls or skyrmions that can be shifted by the current in racetrack-based devices^{5,6}. The key challenges are to achieve small bits and translate them at high speed. Tremendous progress has already been made utilizing new materials and physical phenomena. The early focus on in-plane magnetized ferromagnets with wide domain walls (~100 nm) driven by conventional spin-transfer torque² has given way to perpendicularly magnetized ferromagnetic heterostructures in which interfacial spin-orbit coupling stabilizes nanoscale chiral spin textures (~1–10 nm)^{7,8} that are efficiently driven by spin-orbit torques (SOTs)^{5,6}. However, ferromagnets suffer from fundamental limitations that impede further progress: stray-field interactions limit the bit size^{9–12} and precessional dynamics limit the operating speeds^{10,11}.

By contrast, antiferromagnets lack stray fields, which allows for atomically thin domain walls with a high packing density⁹ and sub-10 nm skyrmions with room-temperature stability¹². Antiferromagnets also exhibit much faster dynamics than ferromagnets, with terahertz switching speeds^{4,10,11,13} and relativistic spin texture dynamics¹⁴. Though some methods have been proposed^{15–19}, manipulating and detecting antiferromagnetic spin textures is, unfortunately, challenging. However, in ferrimagnets the opposing sublattices can fully compensate one another to achieve behaviours similar to those of antiferromagnets²⁰, while they remain individually detectable and addressable if the electronic or optical properties of the constituent elements are different.

Here we show that by using ferrimagnets whose magnetization and angular momentum compensation temperatures nearly coincide, the fundamental limitations of ferromagnets can be overcome. We show that the speed limit^{21,22} for current-driven domain

wall motion in ferromagnets does not exist in ferrimagnets with a vanishing angular momentum, and we attain speeds for SOT-driven motion that exceed 1.3 km s⁻¹. We then show that these same materials can host magnetic skyrmions approaching 10 nm in size at room temperature and zero applied field, which until now has only been possible at cryogenic temperatures under fields > 1 T (refs ^{8,23}).

Modelling of ferrimagnetic soliton dynamics

Magnetization dynamics in ferromagnets follows the Landau–Lifshitz–Gilbert equation:

$$\dot{\mathbf{m}} = -\frac{\gamma\mu_0}{1+\alpha^2}\mathbf{m}\times\mathbf{H} + \frac{\gamma\alpha\mu_0}{1+\alpha^2}\mathbf{H}_\perp \quad (1)$$

with γ the gyromagnetic ratio, α the Gilbert damping and \mathbf{m} the magnetization \mathbf{M} normalized by its saturation value M_s . $\mathbf{H} = -\frac{\delta E}{\delta \mathbf{M}}$ is the effective magnetic field, including applied and internal contributions, with $\mathbf{H}_\perp = -\mathbf{m}\times(\mathbf{m}\times\mathbf{H})$ the component perpendicular to \mathbf{m} . The first term in equation (1) causes precession around \mathbf{H} , and the weaker dissipative term slowly brings \mathbf{m} towards \mathbf{H} . This indirect mechanism often limits switching and domain wall speeds in ferromagnets.

In the case of ferrimagnets with strongly exchange-coupled antiparallel sublattices, equation (1) can be adapted by renormalizing γ and α to²⁴:

$$\gamma \rightarrow \gamma' = \frac{M_s(T)}{S(T)} \quad (2)$$

$$\alpha \rightarrow \alpha' = \frac{S_0}{S(T)} \quad (3)$$

¹Department of Materials Science and Engineering, Massachusetts Institute of Technology, Cambridge, MA, USA. ²Max-Born-Institut, Berlin, Germany.

³Institut für Optik und Atomare Physik, Technische Universität Berlin, Berlin, Germany. ⁴Deutsches Elektronen-Synchrotron (DESY), FS-PE, Hamburg, Germany. ⁵These authors contributed equally: Lucas Caretta, Maxwell Mann, Felix Büttner. *e-mail: gbeach@mit.edu

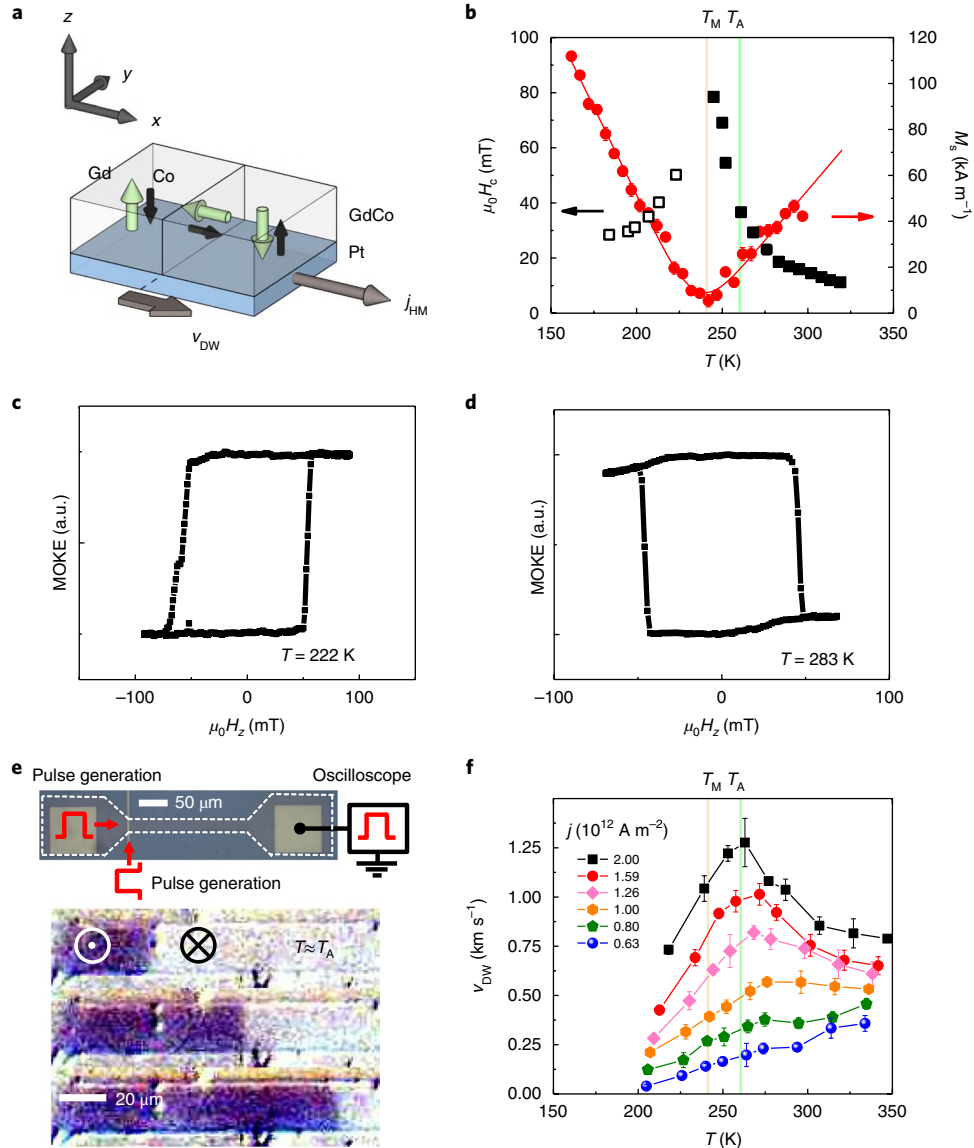


Fig. 1 | Measurement of T_A and T_M . **a**, Schematic of the Pt/Co₄₄Gd₅₆ layer structure in which ferrimagnetic Co₄₄Gd₅₆ exhibits a perpendicular magnetic anisotropy (the TaO_x cap is not shown). Green (black) arrows indicate the Gd (Co) sublattice moments in a domain wall (DW) structure. **b**, Coercivity (squares) and saturation magnetization (circles) as a function of temperature. Open (filled) squares indicate the positive (negative) sign of the MOKE signal at a positive field saturation. **c,d**, Representative MOKE hysteresis loops are measured at $T = 222$ K (**c**) and $T = 283$ K (**d**). **e**, Kerr microscopy images (bottom) showing current-driven domain wall motion near T_A , where a train of N current pulses with amplitude $j_{HM} = 1.5 \times 10^{12}$ A m⁻² was injected between each image frame (top). **f**, v_{DW} as a function of temperature for various current densities. The error bar represents the standard deviation of 5-20 independent measurements of v_{DW} (Supplementary Fig. 9). The sample temperature was corrected for instantaneous heating during the current application (Supplementary Fig. 2). a.u., arbitrary units.

with

$$M_s(T) = |M_{s,1}(T) - M_{s,2}(T)| \quad (4)$$

$$S(T) = \left| \frac{M_{s,1}(T)}{\gamma_1} - \frac{M_{s,2}(T)}{\gamma_2} \right| \quad (5)$$

$$S_0 = \alpha_0 \left(\frac{M_{s,1}(T)}{\gamma_1} + \frac{M_{s,2}(T)}{\gamma_2} \right) \quad (6)$$

where the subscripts denote sublattices, α_0 parametrizes the damping and $\gamma_i = g\mu_B/\hbar$ is the gyromagnetic ratio (with g the Landé g -factor, μ_B the Bohr magneton and \hbar the reduced Planck constant). M_s and stray fields vanish at temperature T_M , which is generally distinct from the angular momentum compensation temperature T_A where the net spin density $S(T) = 0$. Most effective fields scale as $1/M_s(T)$, which suggests that applied torques might become extremely efficient near T_M . However, as $\gamma \propto M_s$, γH remains finite and so no anomalies are expected as $M_s \rightarrow 0$. At T_A , by contrast, both γ and α diverge so that the precessional term in the Landau-Lifshitz-Gilbert equation vanishes to leave:

$$\dot{\mathbf{m}} = \frac{\mu_0 M_s(T)}{S_0} \mathbf{H}_\perp = \frac{1}{S_0} \mathbf{h}_\perp \quad (7)$$

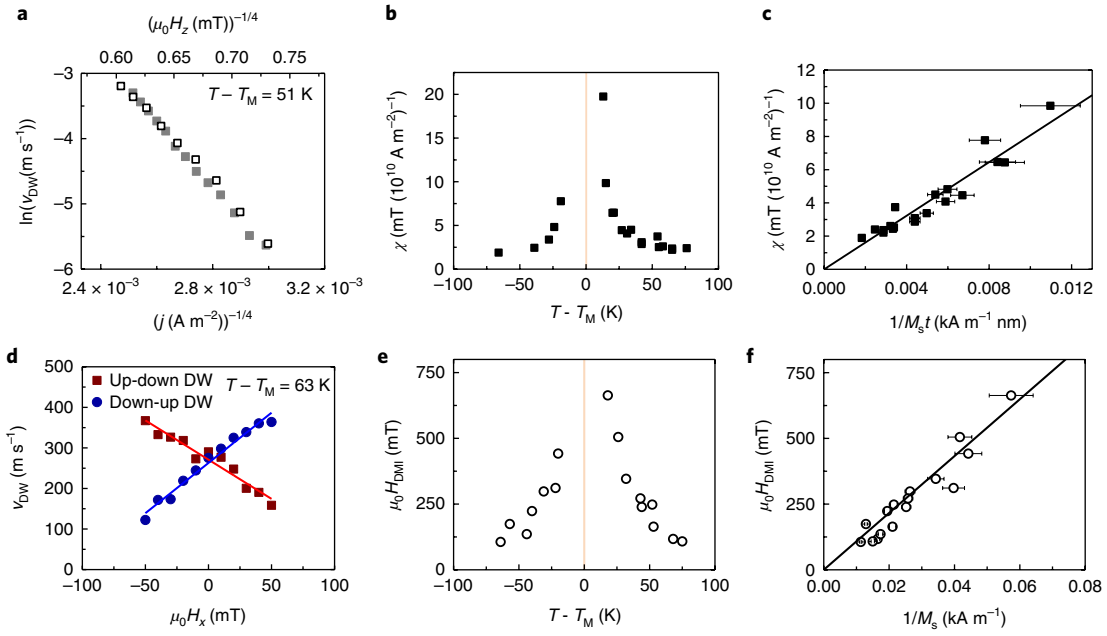


Fig. 2 | SOTs and DMI. **a**, Out-of-plane field- (open squares) and in-plane current- (filled squares) driven v_{DW} in the creep regime. **b**, SOT effective field per unit current density, χ , as a function of temperature T . Divergence occurs at magnetic compensation T_M . **c**, χ plotted as a function of the inverse saturation magnetization M_s^{-1} . **d**, Exemplary v_{DW} as a function of the longitudinal applied field $\mu_0 H_x$ at $T - T_M = 63 \text{ K}$. The $\mu_0 H_x$ intercept of the linear fit gives $\mu_0 H_{DMI}$ (ref. 6). **e**, $\mu_0 H_{DMI}$ as a function of T . Divergence occurs at T_M . **f**, $\mu_0 H_{DMI}$ as a function of M_s^{-1} . Error bars in **e** and **f** are propagated from the $M_s(T)$ fit (Supplementary Fig. 1).

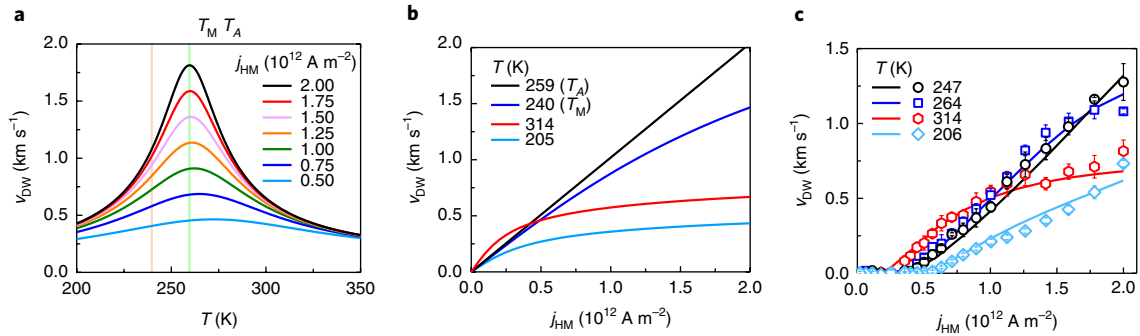


Fig. 3 | Accurate modelling of the temperature and current dependence of v_{DW} . **a**, Terminal v_{DW} as a function of T as predicted by equation (9). The velocity peaks at the angular momentum compensation but does not diverge. Peaks are less pronounced at smaller heavy metal current densities j_{HM} . **b**, The same data as in **a** plotted as a function of j instead of T . Near T_A the velocity $v(j)$ is linear for all j . **c**, Experimental $v(j)$ data (open symbols) overlaid with a full 1D domain wall model (lines), which includes the experimental current pulse shape as well as thermal and pinning effects (Methods and Supplementary Fig. 3). Joule heating leads to a saturation of the data even near $T_A = 260 \text{ K}$ because the device temperature changes during the 1 ns pulse. The reduced de-pinning threshold at elevated temperatures is responsible for the sizable monotonic variation of v with T at small j . Error bar represents the standard deviation of 5 to 20 independent measurements of v_{DW} (Supplementary Fig. 9).

with $\mathbf{h}_\perp = \mu_0 M_s(T) \mathbf{H}_\perp = \delta E / \delta \mathbf{m}$. This fundamentally changes the dynamics of solitons (quasi-particles) such as domain walls and skyrmions. In general, the precession term of the Landau–Lifshitz–Gilbert equation leads to topological gauge terms in the Lagrangian and in the equation of motion of any magnetic soliton²⁵ and ultimately to typical topological dynamics, such as the Walker breakdown of domain walls and the Hall effect^{26,27} and gyration²⁸ of skyrmions. At T_A , all of these effects vanish and magnetic quasi-particles behave like Newtonian particles, that is, they move immediately and rapidly in the direction of the applied force^{12,29,30}, which is highly desirable for many applications.

Fast domain wall motion

We examined spin texture statics and dynamics in $\text{Gd}_{44}\text{Co}_{56}$, an amorphous ferrimagnetic alloy whose antiferromagnetically coupled sublattices (Fig. 1a) possess similar g -factors such that T_A is close to T_M . Perpendicularly magnetized $\text{Ta}(1 \text{ nm})/\text{Pt}(6 \text{ nm})/\text{Gd}_{44}\text{Co}_{56}(6 \text{ nm})/\text{TaO}_x(3 \text{ nm})$ films were sputter deposited on Si/SiO_2 (Methods) with the alloy composition chosen to yield compensation near room temperature. The bottom Pt layer serves as a source of SOT, owing to the spin Hall effect in Pt, and simultaneously generates a strong Dzyaloshinskii–Moriya interaction (DMI). The top TaO_x is a protective cap. Figure 1b shows the temperature (T) dependence of M_s and coercivity $\mu_0 H_c$, obtained by vibrating

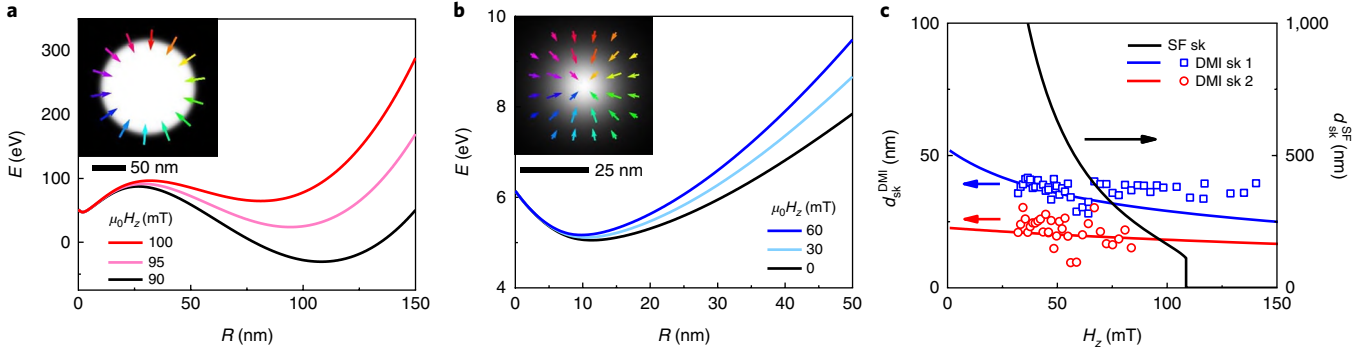


Fig. 4 | Stray-field versus DMI skyrmions. **a,b**, Analytically calculated energy E versus radius R at several applied fields $\mu_0 H_z$. Shown are a stray-field skyrmion with parameters typical of heavy metal/ferromagnet multilayers (**a**) and a DMI-stabilized skyrmion with parameters that correspond to Pt/Gd₄₄Co₅₆/TaO_x (**b**) (Methods). Inset: micromagnetically simulated spin structures at a field of 100 mT in **a**, and at a zero field in **b**; the arrows in **b** refer to one of the sublattices. **c**, Calculated skyrmion diameter d_{sk} versus $\mu_0 H_z$ for the stray-field (SF) skyrmion (sk) in **a** and for the DMI skyrmion in **b**. The solid blue curve was calculated using the material parameters except for the anisotropy, which was 16 kJ m⁻³. Open symbols are experimental data for two skyrmions whose size difference can be accounted for by a difference in local anisotropy.

sample magnetometry and magneto-optical Kerr effect (MOKE) polarimetry, respectively. Figure 1c,d shows representative out-of-plane MOKE hysteresis loops. $M_s(T)$ vanishes and $H_c(T)$ diverges at $T \approx 240$ K, which identifies this temperature as T_M . The MOKE contrast inverts across T_M as expected, because it arises primarily from the Co sublattice, which is parallel (antiparallel) to the net magnetization above (below) T_M .

Domain wall motion was studied in lithographically patterned tracks using wide-field Kerr microscopy. Figure 1e shows a series of Kerr snapshots acquired as nanosecond current pulses were injected to drive a domain wall along the track (Methods). Both up-down and down-up domain walls move along the current flow direction, consistent with SOT-driven left-handed Néel domain walls^{5,6,22}. Figure 1f shows domain wall velocity (v_{DW}) versus T for several current densities j_{HM} in the Pt layer. The $v_{DW}(T)$ curves are shifted horizontally to account for Joule heating (Supplementary Figs. 2 and 3). At a low current, v_{DW} increases monotonically with T , whereas at a larger current v_{DW} exhibits a pronounced peak at $T \approx 260$ K, significantly above T_M .

The SOT and DMI effective fields diverge at T_M and not at the velocity peak, which implies that their divergence is not responsible for the dramatic velocity enhancement in Fig. 1f. This was experimentally verified—Fig. 2a shows the field- and current-driven v_{DW} in the creep regime (Supplementary Figs. 4 and 5), in which identical scaling is observed in both cases. The current hence acts like an easy-axis effective field $H_z^{eff} = \chi j_{HM}$, as expected for damping-like SOT acting on Néel domain walls. In that case²¹, $\chi = \frac{\pi}{2} \frac{\hbar \theta_{SH}^{eff}}{2e\mu_0 M_s t}$, with t the magnetic film thickness, e the electron charge and θ_{SH}^{eff} the effective spin Hall angle. Figure 2b,c shows that $\chi(T)$ scales as $1/M_s(T)$, as expected from theory and previous studies^{31–35}, from which we determine that $\theta_{SH}^{eff} = 0.155$, which is nearly independent of temperature in this range. Harmonic SOT measurements are consistent with these results (Supplementary Figs. 6f and 7).

The domain wall chirality and DMI effective field H_{DMI} can be obtained from the dependence of v_{DW} on longitudinal field H_x (ref. 9). SOT-driven v_{DW} increases (decreases) when H_x is parallel (antiparallel) to H_{DMI} , which sets the orientation of the Néel domain walls. The measured positive (negative) slopes of $v_{DW}(H_x)$ for down-up (up-down) domain walls in Fig. 2d indicate left-handed chirality, both above and below T_M . Extrapolation to $v_{DW} = 0$ yields H_{DMI} , which is related to the DMI parameter D through $H_{DMI} = \frac{D}{\mu_0 M_s \Delta}$ with Δ the domain wall width²². As seen in Fig. 2e,f, H_{DMI} diverges as $1/M_s(T)$ and we find that $D = 0.12$ mJ m⁻² (Methods and Supplementary Fig. 8). This compares well to the DMI values reported for

Pt/ferromagnet systems^{5,6,36,37} and Pt/ferrimagnet systems³⁸, given the differences in t .

The spin Hall effect-driven velocity of chiral domain walls in ferromagnets is given in the one-dimensional (1D) model by²²:

$$v_{FM} = \frac{\gamma}{M_s} \frac{\pi}{2} \frac{D j_{HM}}{\sqrt{j_{HM}^2 + \alpha j_0^2}} \quad (8)$$

where $j_0 = \frac{2e t D}{\hbar \theta_{SH}^{eff} \Delta}$. The velocity first increases linearly with current,

$v_{FM} \approx \frac{\gamma}{\alpha M_s} \frac{\pi}{2} D \frac{j_{HM}}{j_0}$, and eventually saturates towards $v_{sat} = \frac{\gamma}{M_s} \frac{\pi}{2} D$ for $j_{HM} > \alpha j_0$, which serves to limit the domain wall speed. However, in ferrimagnets, α and γ are replaced by $\alpha'(T)$ and $\gamma'(T)$ to yield:

$$v_{FIM} = \frac{\pi}{2} \frac{D j_{HM}}{\sqrt{(S(T) j_{HM})^2 + (S_0 j_0)^2}} \quad (9)$$

which is independent of M_s . Instead, the denominator depends on the net spin density $S(T)$, which vanishes at T_A so that $v(j_{HM})$ does not saturate and so allows very high velocities to be attained.

Equation (9) explains well the $v_{DW}(T)$ curves in Fig. 1f. At a small $j_{HM} \ll j_0$, the velocity is always in the linear regime because $S_0 j_0$ dominates in the denominator. At a larger j_{HM} , the velocity is in the saturation regime except near $T \approx T_A$ where $S(T) = 0$. This leads to a velocity maximum at T_A but with no critical behaviour, consistent with Fig. 1f. We conclude that the velocity peak in Fig. 1f corresponds to $T_A \approx 260$ K. Comparing T_A and T_M yields $g_{Gd} = 2.0$ and $g_{Co} = 2.05$, which are reasonably consistent with values reported for GdCo (ref. 39).

Figure 3a shows $v_{DW}(T)$ calculated from equation (9) for several j_{HM} using experimentally determined parameters and modelling $M_{s,Gd}(T)$ and $M_{s,Co}(T)$ by fitting $M_s(T)$ (Supplementary Section 1). Figure 3b shows the corresponding calculated $v_{DW}(j_{HM})$ curves, which highlight the reason for the enhanced velocities observed near T_A in Fig. 3a. Far from compensation, $v_{DW}(j_{HM})$ increases linearly and then saturates. As T_A is approached, velocity saturation occurs at increasingly high j_{HM} , and when $T = T_A$, $v_{DW}(j_{HM})$ is always linear. Figure 3c shows experimental $v_{DW}(j_{HM})$ curves at various cryostat temperatures, along with fits using the 1D model in which the Joule heating-induced temperature variation and pinning is included (Supplementary Sections 2 and 3). The latter finally explains the monotonic increase of $v_{DW}(T)$ at small j_{HM} . Overall, we

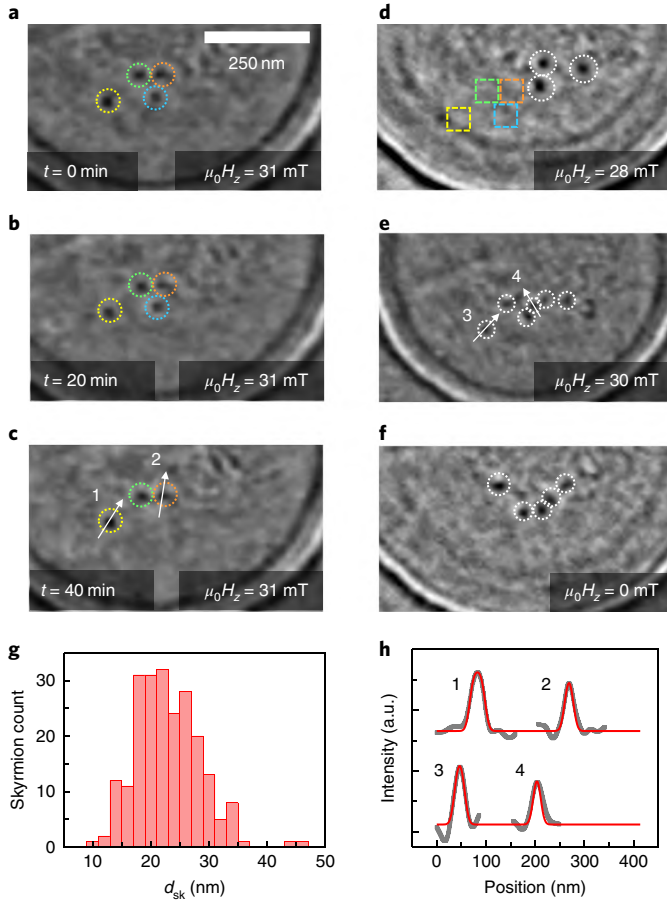


Fig. 5 | Room-temperature-stable ferrimagnetic DMI skyrmions. a–c. Sequence of X-ray holography images of Pt/Co₄₄Gd₅₆/TaO_x immediately after injecting a nucleation current pulse (a), after 20 min (b) and after 40 min (c). Skyrmions are outlined by circles for clarity. **d,e.** Image of skyrmions at different positions obtained after saturating the film and injecting a nucleation current pulse. The coloured squares indicate the absence of skyrmions in locations present in a and b, respectively. **f.** Skyrmions under zero out-of-plane field $\mu_0 H_z$ (nucleated in a bias field which was subsequently reduced to zero). In all the images, the light (dark) contrast indicates magnetization out (into) the plane. The high-pass filter leads to the ringing in some of the images, as seen in f. This is not a magnetic feature but simply an artefact from the circular field of view. **g.** The histogram shows the distribution of skyrmion diameters. **h.** Magnetic contrast line scans of the numbered skyrmions in c and e (grey filled circles) and fits (red lines) (Supplementary Fig. 10).

find that the simple effective ferromagnet model with scaled α and γ agrees well with our experimental data, which implies that it accurately describes the underlying physics.

Small DMI skyrmions

Owing to their weak stray fields, compensated ferrimagnets can also host much smaller room-temperature skyrmions than can ferromagnets¹². So far, room-temperature skyrmions have all been much larger than the 1–10 nm skyrmions seen in single-layer ferromagnets at cryogenic temperatures^{23,40}, with sizes that range from ~30 nm to 2 μ m (refs. ^{36,37,41}). The larger sizes relate to the dominant dipolar interactions in the heavy-metal/ferromagnet multilayers commonly used to realize them¹². This can be understood from the distinct skyrmion energy E versus radius R landscape. Figure 4a shows such a typical $E(R)$ curve, calculated for a ferromagnetic multilayer (Methods). Similar to circular domains in bubble

materials⁴², $E(R)$ exhibits a minimum formed by a balance of stray-field, dipolar and domain wall energies, separated from $R=0$ by a maximum that pushes the equilibrium radius out to larger R . The minimum defines a stray-field skyrmion¹², with a characteristic strong field-dependent size (Fig. 4a,c), collapse at a finite diameter and finite field, and expansion into stripes at zero field. At room temperature, the collapse diameter of such stray-field skyrmions is much larger than 10 nm for realistic material parameters, as described elsewhere¹².

In films with a strong DMI and simple anisotropy-like stray-field interactions, such as atomically thin ferromagnets in which nanometre-scale skyrmions have previously been observed^{8,23}, there is a minimum in $E(R)$ with no intermediate maximum, which allows the equilibrium skyrmion size to be much smaller. This minimum, which defines such DMI skyrmions¹², exists for any applied field but its depth scales with the film thickness¹², which is why ultrasmall ferromagnetic skyrmions^{8,23} cannot be stable at room temperature—and increasing the film thickness leads to destabilizing dipolar fields¹². In addition, surface–volume stray-field interactions in thicker ferromagnets can lead to a non-uniform (twisted) skyrmion profile along the out-of-plane direction^{43,44} and hence additional destabilizing 3D collapse paths⁴⁵.

In compensated ferrimagnets with bulk perpendicular magnetic anisotropy, film thickness can be increased without increasing the stray fields, so the depth of the potential well that stabilizes DMI skyrmions can be increased¹². Figure 4b shows $E(R)$ computed for parameters that correspond to the ferrimagnet studied here (Methods), along with a micromagnetically computed spin structure that shows a compact Néel skyrmion. We predict a zero-field minimum at small R with a depth sufficient for room-temperature stability, and a field-insensitive size characteristic of DMI skyrmions¹², as shown in Fig. 4c. We note that away from T_M , stray fields can destabilize DMI skyrmions. However, as stray-field energies scale with M_s^2 , DMI skyrmions are expected to be stable up to $M_s \approx 150$ kA m⁻¹ in our material, which corresponds to a large temperature range of over 100 K around T_M (Fig. 1b).

These predictions were confirmed by room-temperature imaging in a similar Pt/Gd₄₄Co₅₆/TaO_x film using X-ray holography (Methods). Nanotracks were patterned onto SiN membranes (Methods) to permit current pulse injections for skyrmion nucleation, as has been shown elsewhere^{46–48}. Starting from the out-of-plane saturated state, skyrmions were nucleated by injecting 10 ns current pulses in the presence of an out-of-plane bias field (Methods and Supplementary Fig. 10). Skyrmions appear as circular regions of dark contrast (down magnetization) in the otherwise up-magnetized (light contrast) film. Every image is independently reconstructed by two high-resolution reference holes, and skyrmions are only counted if they meet strict criteria (Supplementary Section 8 and Supplementary Fig. 11). Figure 5a shows an exemplary magnetic contrast image after current-pulse nucleation in which we identify four skyrmions, as indicated by the coloured circles. Figure 5b shows a subsequent image of the same state with the four skyrmions visible at the same locations, which distinguishes them from background intensity fluctuations that vary randomly from image to image. After some time, the skyrmions tend to vanish, with the smallest of the four skyrmions (with a diameter of 16 nm) no longer present after 40 minutes (Fig. 5c). The thermal lifetime of the skyrmions is longer for larger skyrmions, which were observed to persist for several hours in this sample at room temperature.

Skyrmions were observed in a variety of locations and in a broad range of applied fields (Fig. 5a–f). The skyrmions remain stable in a zero applied field, as shown in Fig. 5f. There is almost no correlation between the positions of the skyrmions before and after saturation and renucleation. The coloured squares in Fig. 5d indicate the absence of skyrmions in the locations they appeared in Fig. 5a,b. Also, all of the skyrmions disappear in a field of 450 mT, which clearly distinguishes them from random contrast variations.

The skyrmions range in size (Fig. 5g), with a mean diameter of 23 nm and minimum observed diameters approaching ~10 nm, which is significantly smaller than has been observed in ferromagnets at room temperature. We attribute the distribution in sizes to a dispersion in local magnetic properties. Small variations in anisotropy, for example, lead to a significant variation in the skyrmion size, as seen in the calculated $R(H_z)$ curves in Fig. 4c. The sizes in Fig. 5g were conservatively estimated from the largest possible contour of the black region in the images, which accounts for all of the resolution-limiting effects. In reality, the skyrmions are therefore significantly smaller as the apparent size includes convolution with the instrument resolution. To estimate the minimum skyrmion size more accurately, we compared line scans of pairs of small and large skyrmions (Fig. 5h). The peak intensity of the smaller skyrmion was weaker than that of the larger skyrmion, which provides a measure of size beyond the resolution limit³⁶. Size was estimated by fitting each skyrmion profile to a box function convoluted with a Gaussian of width σ , which represents the domain wall width and the imaging resolution (Supplementary Fig. 10). We identify skyrmions 1–4 (Fig. 5c,e) to be 31 ± 6 , 17 ± 2 , 22 ± 4 and 14 ± 2 nm in diameter, respectively, where the uncertainty comes from noise in the image contrast (Supplementary Fig. 10). Finally, as shown in Fig. 4c, these skyrmions show a flat $R(H_z)$ dependence and are observed in zero and even negative fields, which is a clear signature of DMI skyrmions. We hence conclude that DMI-stabilized skyrmions are stable at room temperature in this material, which would not be possible in a ferromagnet.

Conclusions

We have demonstrated fast SOT-driven domain wall motion with velocities that exceed 1 km s^{-1} and small DMI skyrmions of sizes that approach 10 nm at room temperature in ferrimagnetic Pt/Gd₄₄Co₅₆/TaO_x, which has a strong interfacial DMI due to the Pt underlayer. Our experiments confirm that the dynamics of such a ferrimagnet is accurately described by a simple scaled ferromagnet model, even close to compensation and at extreme velocities, which makes decades of ferromagnetic research applicable to this class of materials. Ferrimagnets are therefore promising for spintronic applications based on small, mobile spin textures. Their properties can be controlled by a range of easily tunable engineering parameters, such as interfaces, annealing and composition. More importantly, they provide a means to realize antiferromagnetic spin systems in which the magnetic state can still be readily detected optically and electrically. Yet, the antiferromagnetic properties of solitonic spin textures, such as skyrmions and domain walls, are realized at two distinct temperatures: at magnetic compensation for the static properties (such as size) and at angular momentum compensation for the dynamics. Ferrimagnets for which T_M and T_A are close together, such as GdCo, are therefore necessary to realize simultaneously all the benefits of ferrimagnets in potential device applications.

Online content

Any methods, additional references, Nature Research reporting summaries, source data, statements of data availability and associated accession codes are available at <https://doi.org/10.1038/s41565-018-0255-3>.

References

- Torreson, J. et al. Neuromorphic computing with nanoscale spintronic oscillators. *Nature* **547**, 428–431 (2017).
- Parkin, S. & Yang, S.-H. Memory on the racetrack. *Nat. Nanotech.* **10**, 195–198 (2015).
- Fert, A., Cros, V. & Sampaio, J. Skyrmions on the track. *Nat. Nanotech.* **8**, 152–156 (2013).
- Olejnik, K. et al. Terahertz electrical writing speed in an antiferromagnetic memory. *Sci. Adv.* **4**, eaar3566 (2018).
- Emori, S., Bauer, U., Ahn, S.-M., Martinez, E. & Beach, G. S. D. Current-driven dynamics of chiral ferromagnetic domain walls. *Nat. Mater.* **12**, 611–616 (2013).
- Ryu, K.-S., Thomas, L., Yang, S.-H. & Parkin, S. Chiral spin torque at magnetic domain walls. *Nat. Nanotech.* **8**, 527–533 (2013).
- Bode, M. et al. Chiral magnetic order at surfaces driven by inversion asymmetry. *Nature* **447**, 190–193 (2007).
- Heinze, S. et al. Spontaneous atomic-scale magnetic skyrmion lattice in two dimensions. *Nat. Phys.* **7**, 713–718 (2011).
- Yang, S.-H., Ryu, K.-S. & Parkin, S. Domain-wall velocities of up to 750 m s^{-1} driven by exchange-coupling torque in synthetic antiferromagnets. *Nat. Nanotech.* **10**, 221–226 (2015).
- Jungwirth, T., Marti, X., Wadley, P. & Wunderlich, J. Antiferromagnetic spintronics. *Nat. Nanotech.* **11**, 231–241 (2016).
- Baltz, V. et al. Antiferromagnetic spintronics. *Rev. Mod. Phys.* **90**, 15005 (2018).
- Büttner, F., Lemesch, I. & Beach, G. S. D. Theory of isolated magnetic skyrmions: from fundamentals to room temperature applications. *Sci. Rep.* **8**, 4464 (2018).
- Cheng, R., Xiao, D. & Brataas, A. Terahertz antiferromagnetic spin Hall nano-oscillator. *Phys. Rev. Lett.* **116**, 207603 (2016).
- Shiino, T. et al. Antiferromagnetic domain wall motion driven by spin-orbit torques. *Phys. Rev. Lett.* **117**, 87203 (2016).
- Cheng, R. & Niu, Q. Dynamics of antiferromagnets driven by spin current. *Phys. Rev. B* **89**, 81105 (2014).
- Hirata, Y. et al. Correlation between compensation temperatures of magnetization and angular momentum in GdFeCo ferrimagnets. *Phys. Rev. B* **97**, 220403(R) (2018).
- Kim, S. K., Tchernyshyov, O. & Tserkovnyak, Y. Thermophoresis of an antiferromagnetic soliton. *Phys. Rev. B* **92**, 20402 (2015).
- Zhang, X., Zhou, Y. & Ezawa, M. Antiferromagnetic skyrmion: stability, creation and manipulation. *Sci. Rep.* **6**, 24795 (2016).
- Barker, J. & Tretiakov, O. A. Static and dynamical properties of antiferromagnetic skyrmions in the presence of applied current and temperature. *Phys. Rev. Lett.* **116**, 147203 (2016).
- Kim, K.-J. et al. Fast domain wall motion in the vicinity of the angular momentum compensation temperature of ferrimagnets. *Nat. Mater.* **16**, 1187–1192 (2017).
- Thiaville, A., Rohart, S., JuéÉ., Cros V. & Fert A.. Dynamics of Dzyaloshinskii domain walls in ultrathin magnetic films. *Europhys. Lett.* **100**, 57002 (2012).
- Martinez, E., Emori, S., Perez, N., Torres, L. & Beach, G. S. D. Current-driven dynamics of Dzyaloshinskii domain walls in the presence of in-plane fields: full micromagnetic and one-dimensional analysis. *J. Appl. Phys.* **115**, 213909 (2014).
- Romming, N. et al. Writing and deleting single magnetic skyrmions. *Science* **341**, 636–639 (2013).
- Wangness, R. K. Sublattice effects in magnetic resonance. *Phys. Rev.* **91**, 1085–1091 (1953).
- Tchernyshyov, O. Conserved momenta of a ferromagnetic soliton. *Ann. Phys.* **363**, 98–113 (2015).
- Litzius, K. et al. Skyrmion Hall effect revealed by direct time-resolved X-ray microscopy. *Nat. Phys.* **13**, 170–175 (2017).
- Jiang, W. et al. Direct observation of the skyrmion Hall effect. *Nat. Phys.* **13**, 162–169 (2017).
- Büttner, F. et al. Dynamics and inertia of skyrmionic spin structures. *Nat. Phys.* **11**, 225–228 (2015).
- Woo, S. et al. Current-driven dynamics and inhibition of the skyrmion Hall effect of ferrimagnetic skyrmions in GdFeCo films. *Nat. Commun.* **9**, 959 (2018).
- Zhang, X., Zhou, Y. & Ezawa, M. Magnetic bilayer-skyrmions without skyrmion Hall effect. *Nat. Commun.* **7**, 10293 (2016).
- Ueda, K., Mann, M., Pai, C.-F., Tan, A.-J. & Beach, G. S. D. Spin-orbit torques in Ta/Tb_xCo_{100-x} ferrimagnetic alloy films with bulk perpendicular magnetic anisotropy. *Appl. Phys. Lett.* **109**, 232403 (2016).
- Seung Ham, W. et al. Temperature dependence of spin-orbit effective fields in Pt/GdFeCo bilayers. *Appl. Phys. Lett.* **110**, 242405 (2017).
- Roschewsky, N., Lambert, C.-H. H. & Salahuddin, S. Spin-orbit torque switching of ultralarge-thickness ferrimagnetic GdFeCo. *Phys. Rev. B* **96**, 64406 (2017).
- Mishra, R. et al. Anomalous current-induced spin torques in ferrimagnets near compensation. *Phys. Rev. Lett.* **118**, 167201 (2017).
- Je, S.-G. G. et al. Spin-orbit torque-induced switching in ferrimagnetic alloys: experiments and modeling. *Appl. Phys. Lett.* **112**, 62401 (2018).
- Moreau-Luchaire, C. et al. Additive interfacial chiral interaction in multilayers for stabilization of small individual skyrmions at room temperature. *Nat. Nanotech.* **11**, 444–448 (2016).

37. Woo, S. et al. Observation of room-temperature magnetic skyrmions and their current-driven dynamics in ultrathin metallic ferromagnets. *Nat. Mater.* **15**, 501–506 (2016).
38. Tono, T. et al. Chiral magnetic domain wall in ferrimagnetic GdFeCo wires. *Appl. Phys. Express* **8**, 73001 (2015).
39. Binder, M. et al. Magnetization dynamics of the ferrimagnet CoGd near the compensation of magnetization and angular momentum. *Phys. Rev. B* **74**, 134404 (2006).
40. Romming, N., Kubetzka, A., Hanneken, C., von Bergmann, K. & Wiesendanger, R. Field-dependent size and shape of single magnetic skyrmions. *Phys. Rev. Lett.* **114**, 117203 (2015).
41. Jiang, W. et al. Blowing magnetic skyrmion bubbles. *Science* **349**, 283–286 (2015).
42. Bogdanov, A. N. Magnetic domains. The analysis of magnetic microstructures. *Low Temp. Phys.* **25**, 151–152 (1999).
43. Dovzhenko, Y. et al. Magnetostatic twists in room-temperature skyrmions explored by nitrogen-vacancy center spin texture reconstruction. *Nat. Commun.* **9**, 2712 (2018).
44. Legrand, W. et al. Hybrid chiral domain walls and skyrmions in magnetic multilayers. *Sci. Adv.* **4**, eaat0415 (2018).
45. Milde, P. et al. Unwinding of a skyrmion lattice by magnetic monopoles. *Science* **340**, 1076–1080 (2013).
46. Büttner, F. et al. Field-free deterministic ultrafast creation of magnetic skyrmions by spin-orbit torques. *Nat. Nanotech.* **12**, 1040–1044 (2017).
47. Hrabec, A. et al. Current-induced skyrmion generation and dynamics in symmetric bilayers. *Nat. Commun.* **8**, 15765 (2017).
48. Legrand, W. et al. Room-temperature current-induced generation and motion of sub-100 nm skyrmions. *Nano. Lett.* **17**, 2703–2712 (2017).

Acknowledgements

Work at MIT was supported by the US Department of Energy, Office of Science, Basic Energy Sciences under award no. DE-SC0012371 (X-ray holography materials growth, device fabrication and imaging), and by the DARPA TEE program

(current-induced dynamics experiments, modelling and skyrmion size analysis). Devices were fabricated using equipment in the MIT Microsystems Technology Laboratory and the MIT Nanostructures Laboratory. The authors thank L. Liu for use of the ion milling equipment. L.C. acknowledges financial support from the NSF Graduate Research Fellowship Program and from the GEM Consortium. F.B. thanks the DFG for funding under grant no. BU 3297/1-1. The authors thank C. Avci, A.J. Tan and M. Huang for discussions.

Author contributions

G.S.D.B. proposed and supervised the study. L.C., M.M., F.B. and G.S.D.B. designed the experiments. L.C. and M.M. designed the measurement apparatus and performed domain wall experiments. C.M. and D.B. designed the high-voltage pulse generator. K.U. optimized the GdCo film growth and deposited the samples. L.C. and M.M. performed lithographic steps for the domain wall tracks and F.B., C.M.G., A.C., D.E. and M.S. prepared and characterized the holography samples. F.B., B.P., C.M.G., P.H., A.C. and C.K. performed the X-ray holographic imaging with the assistance of K.B., and with input and supervision from S.E. P.H. reconstructed the holographic images. F.B. performed all the micromagnetic simulations and analytical calculations. All of the authors participated in the discussion and interpreted the results. L.C., F.B., M.M. and G.S.D.B. drafted the manuscript. All authors commented on the manuscript.

Competing interests

The authors declare no competing interests.

Additional information

Supplementary information is available for this paper at <https://doi.org/10.1038/s41565-018-0255-3>.

Reprints and permissions information is available at www.nature.com/reprints.

Correspondence and requests for materials should be addressed to G.S.D.B.

Methods

Model calculations. For the 1D model simulations, we numerically solved the full 1D model of SOT-driven domain wall motion introduced by Martinez et al.²², with variable γ and α . In time steps of 50 ps, we updated the current density based on the Gaussian pulse shape and the local sample temperature based on the experimentally determined heating and cooling rates (Supplementary Fig. 2). The time-averaged velocities are defined as distance travelled divided by the experimentally determined effective pulse width (Supplementary Fig. 9).

The analytical calculations of skyrmion energy versus radius (Fig. 4a,b) and skyrmion diameter versus out-of-plane field (Fig. 4c) were computed using a published model¹². Figure 4a was derived using a multilayer with 30 repeats, where each repeat is 4 nm thick and contains a 1 nm thick magnetic layer with the parameters: $A = 10 \text{ pJ m}^{-1}$, $K_u = 824 \text{ kJ m}^{-3}$ (corresponding to an in-plane saturation field of $\mu_0 H_k = 0.7 \text{ T}$), $M_s = 900 \text{ kA m}^{-1}$ and $D = -1 \text{ mJ m}^{-2}$. Here, K_u is the uniaxial anisotropy energy and $\mu_0 H_k$ is the anisotropy field. Figure 4b corresponds to a single 6 nm thick ferrimagnet with $A = 7 \text{ pJ m}^{-1}$, $K_u = 25 \text{ kJ m}^{-3}$, $M_s = 50 \text{ kA m}^{-1}$ and $D = -0.3 \text{ mJ m}^{-2}$. Here we used a local anisotropy that reproduces the field-dependent size of the small skyrmion in Fig. 4c; small variations in anisotropy lead to variations in skyrmion size (Fig. 4c) but not the qualitative shape of the $E(R)$ curve. The insets in Fig. 4a,b were computed with the same material parameters as used in the model calculations, using the MicroMagnum micromagnetic simulation package^{37,49} with cell sizes of $1 \text{ nm} \times 1 \text{ nm} \times 120 \text{ nm}$ and $0.5 \text{ nm} \times 0.5 \text{ nm} \times 6 \text{ nm}$, respectively. All of the calculations employ effective medium scaling to combine all the magnetic sublattices and non-magnetic spacers into one micromagnetic unit³⁷. The skyrmion profiles in the micromagnetic simulations agree with the analytically calculated results, as also shown elsewhere¹².

Sample preparation. The Ta(1)/Pt(6)/Gd₄₄Co₅₆(6)/TaO_x(3) and Ta(1)/Pt(6)/Gd₄₄Co₅₆(12)/TaO_x(3) (thicknesses in nm) samples were grown using d.c. magnetron sputtering at a nominal room temperature with an Ar sputter gas pressure of 3 mtorr and a background base pressure of $\sim 2 \times 10^{-7}$ torr. Samples were deposited on thermally oxidized Si wafers. We neglected current shunting through the Ta seed layer, as the resistivity of Ta is approximately ten times higher than in Pt. GdCo was co-deposited using separate Co and Gd targets, and the composition was controlled by varying the Gd sputter gun current. Deposition rates were calibrated using X-ray reflectivity measurements of the film thickness. The domain wall motion wires and Hall crosses were patterned using photolithography and ion milling. The contact pads (Ta(5 nm)/Au(100 nm)) and Hall cross structures were patterned using standard lift-off processes. SOT effective-field measurements were performed on a $200 \times 40 \mu\text{m}^2$ track and domain wall motion measurements were performed on a nearby $50 \times 40 \mu\text{m}^2$ track. Holography samples were prepared by defining $10 \mu\text{m}$ -wide tracks of the same Ta(1)/Pt(6)/Gd₄₄Co₅₆(6)/TaO_x(3) material as before on a 700 nm thick SiN membrane supported by a high-purity Si frame via electron beam lithography and lift-off. Cr(5 nm)/Au(100 nm) contacts were subsequently deposited by thermal evaporation and shadow masking. On the back side of the membrane we deposited an opaque layer of (Cr(5 nm)/Au(55 nm))₂₀, in which we prepared a holography mask with four holes by focused ion beam milling: one object hole $1 \mu\text{m}$ in diameter and three reference holes with diameters of 30 nm, 40 nm and 100 nm. In a final step, the $10 \mu\text{m}$ wide magnetic track was reduced to 900 nm in the region behind the object hole (Supplementary Fig. 10) and a small notch was introduced to assist the current-induced nucleation of skyrmions⁴⁶.

MOKE measurements. All polar laser MOKE and differential MOKE images were acquired in a custom-built Kerr microscope with independent out-of-plane and in-plane field controls and an integrated flow cryostat for the temperature control. Differential wide-field MOKE microscopy was performed using a light-emitting diode white-light source. Focused laser MOKE measurements were used to acquire hysteresis loops, and were performed using a 532 nm diode laser focused to a spot size of $\sim 10 \mu\text{m}$ and attenuated to $\sim 1 \text{ mW}$ to avoid laser heating of the sample⁵⁰.

Sample current injection. High-bandwidth pulses for domain wall motion experiments were delivered to the sample from a custom-built nanosecond pulse

generator via a waveguide. A low duty cycle was used to avoid heat build-up and damage. Domain walls were nucleated using SOT switching of a constricted region of the wire. The velocity of the domain wall was determined by dividing the change in the position of the domain wall (as viewed by MOKE) by the duration of the current pulse (Supplementary Fig. 9).

Extraction of D and exchange constant. D is extracted from the high current saturation velocity $v_D = \frac{\pi D}{S(T)}$, far from T_A . This yields $D = 0.12 \text{ mJ m}^{-2}$. Next, we determined the domain width $\Delta = 11 \text{ nm}$ from $H_{\text{DMI}} = \frac{D}{\mu_0 M_s \Delta}$, and we used $\Delta = \sqrt{A / K_{\text{eff}}}$ with $K_{\text{eff}} = 1/2 \mu_0 M_s^2$ to extract the exchange stiffness $A = 7 \text{ pJ m}^{-1}$, which is in agreement with the literature values⁵¹. Finally, note that we calculated A using the value of Δ at T_M , where $K_{\text{eff}} \approx K_u$ as $M_s(T = T_M) = 0$. However, Δ shows only very small changes as a function of T due to the small value of M_s in the ferrimagnet for all T (Supplementary Fig. 8), which makes this analysis universally robust.

v_{DW} measurement. Measurements of v_{DW} were made using a wide-field Kerr microscope with in situ field, current and temperature controls. Velocities are defined as the displacement of a domain wall after a single pulse divided by the pulse duration, with the latter calibrated as described in Supplementary Fig. 9. Every velocity data point in this paper represents an average of 4–30 single velocity measurements that correspond to a total domain wall travel distance of $\sim 20 \mu\text{m}$.

X-ray holography. Fourier transform X-ray holography measurements were carried out at room temperature in the custom MAXI endstation at the P04 beamline of the PETRA III synchrotron radiation source, Germany, using a monolithic sample-mask approach^{52–54}. Exploiting X-ray magnetic circular dichroism at the Co L₃ absorption edge at 777.7 eV photon energy, difference holograms obtained with opposite circular polarization encode the Co magnetization map of the sample in the $1 \mu\text{m}$ diameter circular field of view, and the sample topography was also accessible through the local absorption via the sum hologram. Image reconstruction was carried out by direct Fourier inversion and propagation to focus the image⁵⁵. All of the holography images are cropped to the most interesting part of the nanotrack (Supplementary Fig. 10). Regions of dark (light) contrast indicate magnetization pointing out of the plane (into the plane). Skyrmions were nucleated by first saturating the magnetization out of plane and subsequently injecting a single up–down–up current pulse of 10 ns width per polarity and $1.7 \times 10^{12} \text{ A m}^{-2}$ amplitude, with an out-of-plane bias field $B_z \approx 30 \text{ mT}$ along the saturating field direction.

Data availability

The data that support the findings of this study are available from the corresponding author upon reasonable request.

References

49. *Fast Micromagnetic Simulator for Computations on CPU and Graphics Processing Unit* (MicroMagnum, 2013); <http://micromagnum.informatik.uni-hamburg.de/>.
50. Bauer, U., Emori, S. & Beach, G. S. D. Voltage-controlled domain wall traps in ferromagnetic nanowires. *Nat. Nanotech.* **8**, 411–416 (2013).
51. Hansen, P. & Heitmann, H. Media for erasable magneto-optic recording. *IEEE Trans. Magn.* **25**, 4390–4404 (1989).
52. Eisebitt, S. et al. Lensless imaging of magnetic nanostructures by X-ray spectro-holography. *Nature* **432**, 885–888 (2004).
53. Büttner, F. in *Holographic Materials and Optical Systems* (eds Neydenova, I., Babeva, T. & Nazarova, D.) Ch. 10 (InTech, London, 2017).
54. Pfau, B. & Eisebitt, S. in *Synchrotron Light Sources and Free-Electron Lasers* (eds Jaeschke, E., Khan, S., Schneider, J.R. Hastings, J.B.) 1093–1133 (Heidelberg, Springer, 2016).
55. Guehrs, E. et al. Wavefield back-propagation in high-resolution X-ray holography with a movable field of view. *Opt. Express* **18**, 18922–18931 (2010).